PAPER

CrossMark
click for updates

Simultaneously improved electrical properties of crystalline YbAl₃ thin films prepared by co-sputtering technique†

Ran-Ran Li, Dan-Qi He, Xin Mu, Hong-Yu Zhou, Ping Wei,* Wan-Ting Zhu, Xiao-Lei Nie, Wen-Yu Zhao* and Qing-Jie Zhang

With the growing interest in developing miniaturized thermoelectric devices, there has been a strong demand in preparing thermoelectric thin films with high electrical conductivity and large power factors, hence ensuring the miniaturized devices have large cooling capacity and large output powers. This work demonstrated the preparation of intermetallic YbAl₃ thin films through a double-target magnetron co-sputtering technique and a subsequent annealing treatment. It was revealed that the subsequent heat treatment of thin films plays a critical role in achieving crystalline, stoichiometric, and nanostructured YbAl₃ thin films. Benefiting from the significantly improved crystallinity and stoichiometry, the optimized YbAl₃ thin films exhibit extraordinarily high electrical conductivity reaching 1.7×10^6 S m^{-1} and large power factors around 7.4 mW m^{-1} K^{-2}. The figure of merit ZT of the annealed thin films is comparable with that of the bulk materials, showing their potential use in miniaturized thermoelectric devices.

Introduction

Thermoelectric (TE) devices enable direct energy conversion between heat and electricity, which provides a scalable, reliable, and environmental friendly solution for energy conversion applications such as recycling utilization of industrial waste heat and automobile exhaust heat, full-spectrum solar power generation, and high-efficiency cooling of next-generation integrated circuits.[1,2] The conversion efficiency (η) of TE devices is determined by the Carnot efficiency $(T_H - T_C)/T_H$ and the dimensionless figure of merit of TE materials $ZT = \alpha^2\sigma T/\kappa$ through $\eta = (T_H - T_C)/T_H \times (\sqrt{1+ZT} - 1)/(\sqrt{1+ZT} - 1 + T_C/T_H)$, where T_H and T_C are the temperatures at the hot end and the cold one, α is the Seebeck coefficient, σ is the electrical conductivity, T is the average temperature, and κ is the thermal conductivity of TE materials, which is composed of an electronic component (κ_E) and a lattice one (κ_L).[3] Developing high-performance TE materials has been the main objective in the TE community. TE materials including Bi₂Te₃,[4,5] CoSb₃,[6] half-Heusler alloys,[7] PbTe,[8,9] and Mg₂(Si,Sn),[10,11] have been used to fabricate bulk TE devices.

In recent years, the miniaturization of TE devices has been a rapidly growing subject because of their potential applications in integrated circuit, compacted electronic devices, wearable electronics, and microsensors.[12,13] Compared with bulk TE

devices, miniaturized TE devices have advantages of not only small size and light weight, but also higher power density and higher output voltage even at small temperature difference.[14,15] However, when the dimension of bulk materials is decreased to μm or sub-μm thin, the electrical resistance (R) will be increased by orders of magnitude, which leads to lowered maximum cooling capacity (Q_{max}) and maximum output power (P_{max}) since $Q_{max} = \alpha^2 T_H^2/2R$ and $P_{max} = \alpha^2(T_H - T_C)^2/4R$.[16,17] Meanwhile, the high-R thin films generate more Joule heat during operation, bringing additional issues to the device thermal management. The high-R of thin films becomes a bottleneck in developing miniaturized TE devices especially when most of the TE materials have merely moderate σ.

YbAl₃ has attracted considerable attention in recent years due to its exhibiting good TE properties in the low temperature range. YbAl₃ crystallizes in a cubic AuCu₃-type structure with $Pm\bar{3}m$ crystal symmetry. Al atoms locate at the face-center site and Yb atoms occupy the eight vertices of the unit cell. As an intermetallic compound, YbAl₃ displays metallic conduction behavior with extremely high σ.[18] At the same time, YbAl₃ is also a heavy-fermion compound. The hybridization and strong correlation of Yb 4f electrons with the conduction electrons ensure this compound considerably large α in a wide temperature range. Therefore, YbAl₃ possesses extremely high power factor ($\alpha^2\sigma$) which is about three times higher than that of optimized Bi₂Te₃ alloys (one of the state-of-the-art TE materials). The intrinsic features imply that YbAl₃ is a promising TE material for miniaturized TE devices. However, the present studies on YbAl₃ focus mainly on how to optimize the TE performance of YbAl₃ bulk materials through doping or filling,[19-22] the TE transport behavior

research of $YbAl_3$ thin films was still hampered because of the great challenge in thin film preparation.[23]

Here we report for the first time the transport properties of $YbAl_3$ thin films prepared by a co-sputtering technique and a subsequent annealing treatment. The evolution of crystallinity, stoichiometry, and microstructure of $YbAl_3$ thin films during the annealing treatment was investigated. The results indicated that at the optimized annealing condition, the annealed $YbAl_3$ thin films exhibited outperformed electrical transport properties with high electrical conductivity and high power factor. The figure of merit ZT of the annealed thin films was comparable with that of the bulk materials, implying large potential use in the miniaturized TE devices.

Experimental

$YbAl_3$ thin films were prepared by a co-sputtering technique. The whole process includes preparation of $YbAl_3$ and Al targets and co-sputtering process of $YbAl_3$ thin films. $YbAl_3$ and Al targets were prepared by a combination of melt-annealing and plasma active sintering (PAS) methods. Highly pure Yb (99.9%, pellet) and Al (99.999%, powder) with a ratio of 1 : 3 were loaded into a graphite crucible and then sealed into a silica tube under vacuum. The sealed tube was then transferred into a furnace, heated up to 1073 K, and hold for 10 h at 1073 K, then followed by quenching. The quenched ingot was manually milled into powders and annealed for 120 h at 898 K. $YbAl_3$ target was made by sintering the annealed powders using a PAS system at 873 K for 8 min with a vertical pressure of 25 MPa. Al target was prepared by the similar procedure.

$YbAl_3$ thin films were deposited on glass substrates under the Ar atmosphere by a three-target co-sputtering system. Before deposition, the glass substrates were ultrasonically cleaned in alcohol and treated in a radio frequency plasma cleaner. During the sputtering process, the base vacuum was fixed at 4×10^{-4} Pa and the substrate temperature was kept at 673 K. The power applied on $YbAl_3$ target was 40 W and the voltage applied on Al target was 450 V. The working pressure was controlled at around 2 Pa. The film thicknesses were monitored by a quartz crystal sensor. The as-prepared $YbAl_3$ thin films were loaded into a tubular furnace and annealed for 4 h in the temperature range of 723–873 K under the H_2 atmosphere.

The constituent phases of all the thin films were determined by powder X-ray diffraction (XRD, PANalytical X'Pert Pro) with CuK_α radiation ($K_\alpha = 0.15418$ nm). Microstructures and chemical compositions of $YbAl_3$ thin films were examined with field emission scanning electron microscope (FESEM, Zeiss Ultra Plus) and electron probe micro-analyzer (EPMA, JEOL 8230). The uncertainty of EPMA chemical compositions was within $\pm 1\%$. The surface roughness (R_a) and thickness (t) of $YbAl_3$ thin films were examined with a three-dimensional (3D) surface profilometer (NanoMap, 500LS). The distribution of α on the surface of thin films was characterized by Potential-Seebeck Microprobe (PSM, Panco) with an uncertainty of $\pm 10\%$. σ and α were measured using the standard four-probe method (Ulvac. Inc., ZEM-3) in the He atmosphere. The uncertainties were about $\pm 5\%$. Hall coefficient (R_H) was measured by van der Pauw method with a Hall measurement system (Accent 5500) at room temperature. The carrier concentration (n) and Hall mobility (μ_H) were calculated with the equations $n = 1/(R_H q)$ and $\mu_H = |R_H|\sigma$, where q is the free electron charge. Electronic thermal conductivity was calculated from σ according to the Wiedemann–Franz law $\kappa_E = L_0 T\sigma$, where the Lorenz number L_0 has a numerical value 2.0×10^{-8} V^2 K^{-2}.

Results and discussion

The as-prepared $YbAl_3$ thin films labeled as BF673 were obtained on the condition that the substrate temperature was 673 K. The BF673 thin films were annealed for 4 h at different temperatures including 723, 748, 773, 798, 823, and 873 K, which were labeled as AF723, AF748, AF773, AF798, AF823, and AF873, respectively. The thicknesses for the $YbAl_3$ thin films as listed in Table 1 are in the range 600–800 nm. Fig. 1 shows the XRD patterns of $YbAl_3$ thin films. For the BF673 thin films, all the diffraction peaks can be indexed to JCPDS 65-0957 of $YbAl_3$, indicating the starting formation of $YbAl_3$ during the co-sputtering process when the substrate temperature was 673 K. The main phase of the annealed films is $YbAl_3$ and a secondary phase Al was detected in the annealed thin films except AF873. The diffraction intensities of the characteristic peaks of Al increase gradually with increasing the annealing temperature, suggesting the increase of Al content. Note that the diffraction peaks of Al disappear for AF873 thin film, which can be associated with the severe melt and volatilization of the thin film at high annealing temperature.

It is very important to examine the crystallinity of the thin films since the preparation of crystalline $YbAl_3$ thin films is a big challenge.[23] The XRD patterns were fitted by Rietveld refinement to extract the diffraction intensity of each profile for

Table 1 EPMA compositions, crystallinity (X_C), thickness (t), surface roughness (R_a), and room-temperature electrical transport properties of $YbAl_3$ thin films before and after annealing at different temperatures

Sample	EPMA	X_C (%)	t (nm)	R_a (nm)	n (cm^{-3})	μ_H (cm^2 V^{-1} s^{-1})	σ (S m^{-1})	α (μV K^{-1})	$\alpha^2\sigma$ (mW m^{-1} K^{-2})
BF673	$YbAl_{3.75}$	42	609	2	9.0×10^{22}	0.72	1.06×10^6	−30.8	1.0
AF723	$YbAl_{3.27}$	60	776	24	1.4×10^{23}	0.49	1.09×10^6	−57.0	3.5
AF748	$YbAl_{3.17}$	69	759	30	2.5×10^{23}	0.42	1.67×10^6	−57.2	5.5
AF773	$YbAl_{3.03}$	79	818	54	3.3×10^{23}	0.32	1.69×10^6	−66.0	7.4
AF798	$YbAl_{2.98}$	69	760	66	4.2×10^{23}	0.23	1.53×10^6	−58.9	5.3
AF823	$YbAl_{2.90}$	53	833	115	4.5×10^{23}	0.20	1.43×10^6	−50.2	3.6

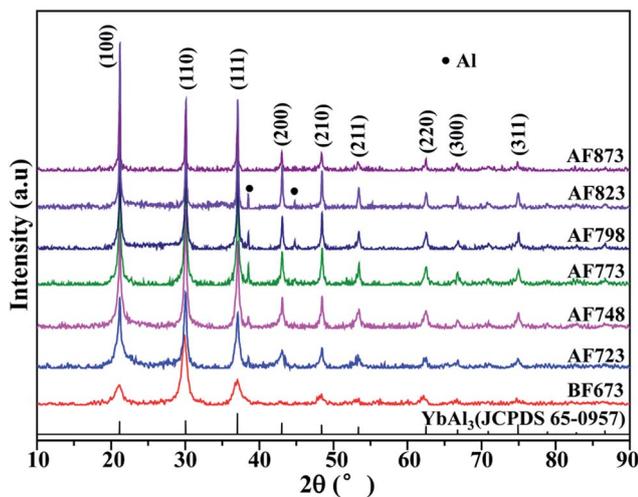**Fig. 1** XRD patterns of YbAl$_3$ thin films before and after annealing at different temperatures.

crystalline YbAl$_3$ and the scattering intensities for amorphous YbAl$_3$. The X_C values of YbAl$_3$ thin films before and after annealing treatment were calculated based on the reference intensity ratio method,[24]

$$X_C = \frac{\sum I_c}{\sum I_c + \sum I_a} \times 100\% \quad (1)$$

where $\sum I_c$ and $\sum I_a$ are the sums of all the diffraction intensities and all the scattering intensities, respectively. The calculated X_C values are listed in Table 1. Before annealing, the X_C value of the as-prepared thin film is only 42%, meaning that the sputtered

thin films are mainly amorphous. After annealed for 4 hours at 723 K, the X_C value of AF723 thin film remarkably increases to ~60%. With increasing the annealing temperature in the range 723–773 K, X_C gradually increases and reaches 79% for AF773 thin film, which suggests that the annealing treatment is very effective in improving the crystallinity. However, as the annealing temperature is further increased, it remarkably decreases to 69% for AF798 and 53% for AF823 thin films.

To explain the abnormal decrease of X_C for the thin films annealed at high temperatures, the chemical composition along the thickness direction of AF773 thin film was investigated with wavelength-dispersive X-ray spectrometer (WDS) as equipped on the EPMA. The measurements were carried out by changing the acceleration voltages of electron beam (U). Here, WDS instead of energy-dispersive X-ray spectrometer (EDS) was used for quantitative analysis of Yb and Al, because EDS cannot distinguish the small energy difference of the characterized lines between Yb (1.53 keV for M$_\alpha$ line) and Al (1.49 keV for K$_\alpha$ line). In order to gather the composition information along the thickness direction, the excitation depths of electron beam at different U were simulated with the Monte Carlo method suggested by Ritchie.[25] As shown in Fig. 2a, the excitation depths of electron beam increase monotonously from 200 nm to 1 μm with increasing the U in the range 8–25 kV. Fig. 2b shows the mole percentages of Al and Yb and Al/Yb atomic ratio of AF773 thin film determined by EPMA at different U. Gradual increase of mole percentage of Yb while reduction of mole percentage of Al and Al/Yb atomic ratio can be found with increasing the U. These results indicate that the content of Al becomes larger and larger while that of Yb becomes smaller and smaller when the detection positions are gradually close to the thin film surfaces.
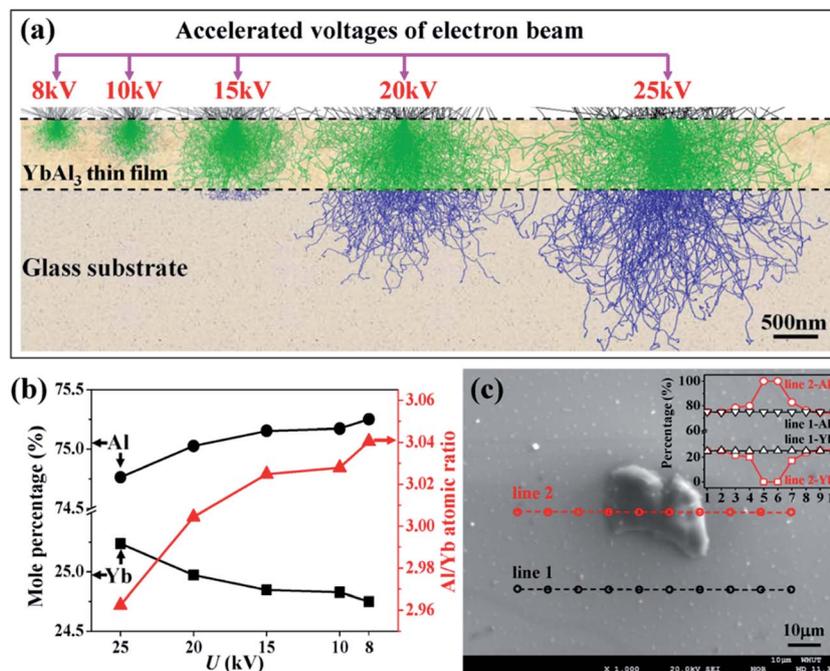

Fig. 2 (a) Excitation depths of electron beam for EPMA at the different accelerate voltages, U. (b) The mole percentages of Al and Yb and Al/Yb atomic ratio of AF773 thin film at different U. (c) FESEM image and EPMA quantitative analysis to determine the chemical composition of a typical bulge precipitated on the surface of AF773 thin film. The quantitative results are given in the insert.

Similar tendency was also found in X-ray photoelectron spectroscopy measurements as given in the ESI (Fig. S1†). The gradient distribution of chemical composition should be attributed to the evaporation of Yb and Al during the annealing process. Since the vapor pressure of Yb (about 5×10^{-3} Pa at its melting point 1273 K) is much higher than that of Al (about 2.42×10^{-20} Pa at its melting point 933 K),[23] the evaporation of Yb should be much easier. Therefore, the abnormal decrease of X_C for the thin films annealed at high temperatures should be attributed to the occurrence of decomposition of $YbAl_3$ and the evaporation of Yb and Al.

Composition analysis indicated that the annealing treatment has a large impact on the stoichiometric composition and crystallinity. Increasing the annealing temperature from 723–773 K leads to increased crystallinity and stoichiometric composition, which is favorable for reaching the most equilibrium state of $YbAl_3$. However, a further increase of annealing temperature will drive $YbAl_3$ to nonequilibrium state with loss of Yb and Al, hence leading to lowered crystallinity.

Fig. 3 shows the surface morphology of the as-prepared and the annealed thin films. For the as-prepared thin film (Fig. 3a), sub-μm-sized particles with 0.2–0.5 μm in diameter and μm-sized coarse particles with several μm in diameter can be observed. The enlarged image (Fig. 3b) shows that these sub-μm- and μm-sized particles in fact are aggregated by numerous spherical nanoparticles which have average diameter only

~30 nm. After annealing, the average size of $YbAl_3$ nanoparticles is enlarged from ~30 nm to ~50 nm as shown in Fig. 3c–h. However, the aggregation of nanoparticles and the formation of coarse particles become more significant with increasing the annealing temperature. For the films annealed at high temperatures such as AF773 and AF823, much larger grains can be found due to the abnormal crystallization and growth of $YbAl_3$ particles.

Fig. 4 shows the 3D images of the surface of $YbAl_3$ thin films. Before annealing, the surface of the as-prepared $YbAl_3$ thin film is flat, indicating a uniform sputtering of thin film. After annealing at 723 K, bulges with several μm in diameter and about 1 μm in height distribute randomly on the surface. With increasing the annealing temperature, their sizes including diameter and height gradually increase. The largest bulges have diameter over 10 μm and the height reaches 3 μm after annealing at 823 K.

In order to clarify the composition of these bulges, EPMA quantitative analysis was performed on the AF773 thin film using a 10 keV acceleration voltage. Fig. 2c shows two individual line scans of WDS with one posed on the flat surface and another crossed a typical bulge. The quantitative results indicate that the composition of the flat surface is $YbAl_3$ with uniform distribution, while the bulge is purely metallic Al. Therefore, the annealing
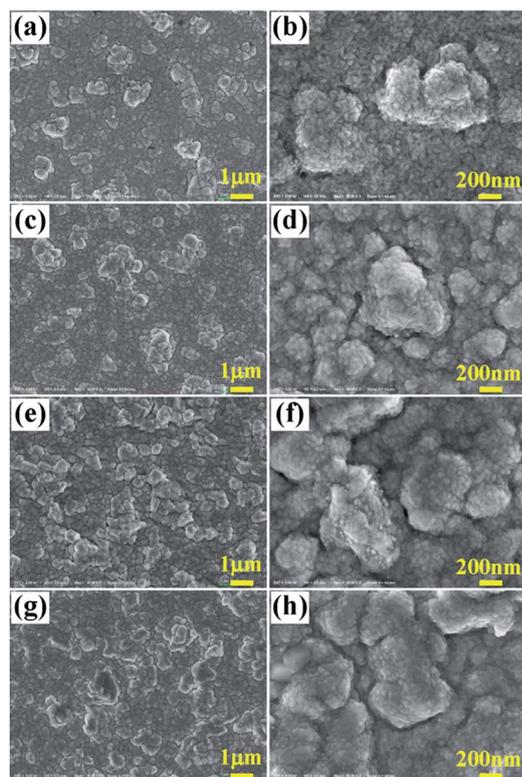

Fig. 3 Surface FESEM images of $YbAl_3$ thin films before and after annealing treatment. (a and b) BF673, (c and d) AF723, (e and f) AF773, and (g and h) AF823.
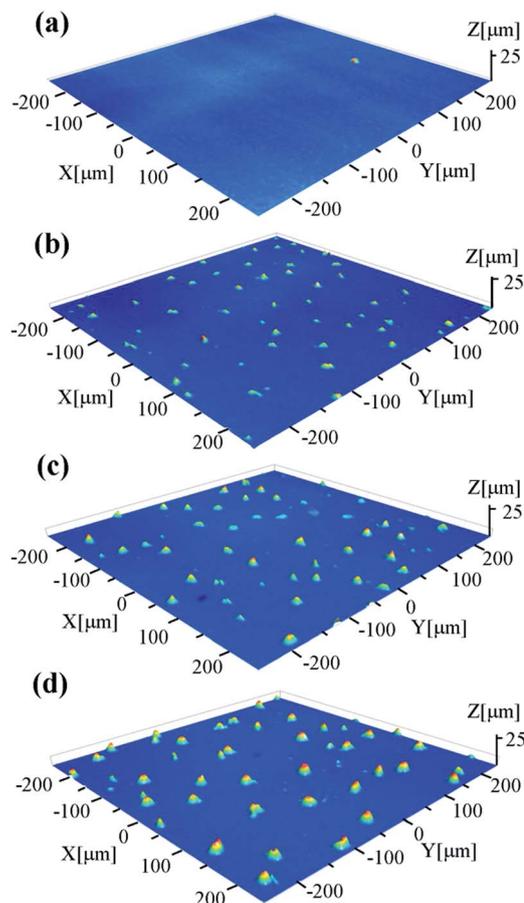

Fig. 4 3D images of the surface of $YbAl_3$ thin films before and after annealing treatment. (a) BF673, (b) AF723, (c) AF773, and (d) AF823.

treatment leads to the precipitation of metallic Al on the surface of YbAl$_3$ thin films.

The precipitation and growth of Al bulges on the film surface should influence the surface roughness R_a. The R_a values of the thin films were determined by a stylus method. For the as-prepared YbAl$_3$ thin film, R_a is only 2 nm, implying the uniform sputtering processing due to the small nanoparticles. After annealing, R_a increases to 24 nm for the AF723 thin film and to 54 nm and 115 nm for the AF773 and AF823 thin films, respectively. Since the growth of nanoparticles is not significant with increasing the annealing temperature in the range 723–823 K, the enlarged R_a should be caused by the aggregation of YbAl$_3$ nanoparticles and the growth of Al bulges. The increased content of Al is consistent with the result detected by XRD. Note that the amount of bulges keeps nearly unchanged at different annealing temperatures, suggesting that the nucleation of the bulges has accomplished even at low annealing temperature. It is indeed highly possible since the melting point of Al nanoparticles can be as low as to 773 K.[26] In fact, the easy loss of Yb and Al at high annealing temperatures is also closely related to the nano-structures in the thin films, which trend to lower the melting point and decomposition temperature of YbAl$_3$ and Al nano-particles with reduced surface energy.

Fig. 5 shows the cross-sectional FESEM images of the thin films. The as-prepared thin film consists of numerous nano-particles, consistent with that observed on the surface. Some amorphous particles are embedded in the thin film, which should be responsible for the low crystallinity (about 42%) as determined by XRD. For the annealed thin films, the less amorphous nanoparticles indicate the increased crystallinity, which is also consistent with the XRD analysis. For the AF773 and AF823 thin films, large grains can be observed on the top of thin film, which should result from the abnormal crystallization of YbAl$_3$ nanoparticles. The abnormal crystallization should be related to the precipitation of Al on the surface. Due to the evaporation of Yb and the precipitation of Al, pores can be found inside the thin films.
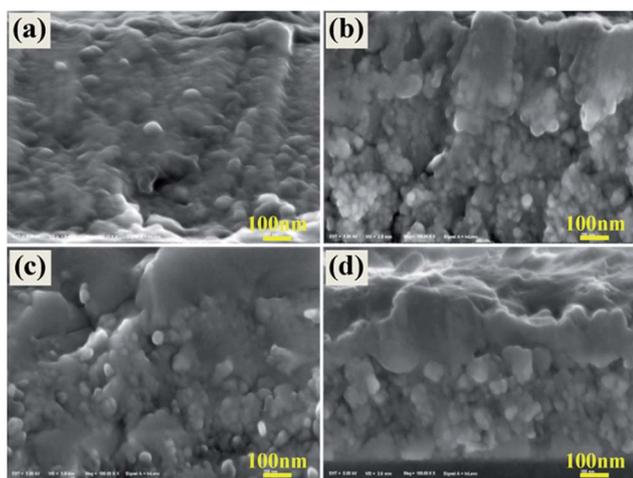
The EPMA compositions of YbAl$_3$ thin films determined by WDS are listed in Table 1. The measurements were performed using a 15 keV acceleration voltage and on flat surfaces, in order to determine the average composition of YbAl$_3$ and avoid detecting the Al bulges. The Al/Yb atomic ratio of BF673 thin film was determined to be 3.75, showing a large deviation from the stoichiometric ratio of YbAl$_3$. The excessive Al in the as-prepared film should be in amorphous phase since no characterized peak of Al was detected from the XRD patterns. Therefore, the amorphous particles observed in Fig. 5a should be a mixture of YbAl$_3$ and Al. After annealing, the Al/Yb atomic ratio significantly decreases into a narrow region spanning from 3.03 to 2.98 when the annealing temperature is in the range 773–798 K, indicating the formation of stoichiometric thin films. Therefore, both crystallinity and stoichiometry have been improved after annealing treatment. The decreased content of Al in YbAl$_3$ with increasing the annealing temperature should be caused by the precipitation of Al on the surface, which inevitably leads to increased Al deficiency.

The distribution of Seebeck coefficient on the surface was characterized to reveal the effect of Al precipitation on the transport properties of YbAl$_3$ thin films. Fig. 6a shows the backscattered electron image of the surface of AF773 thin film. The black spots on the surface are metallic Al bulges. Fig. 6b displays the Seebeck coefficient distribution in the same area where 70×70 measurement points are included. The α values in the flat area fall in the range from -47 to -56 μV K^{-1} with an average value of around -52 μV K^{-1}, which are mainly contributed from YbAl$_3$. The distribution is uniform when considering the measuring uncertainty is around $\pm10\%$. Around the bulges, the α values are 10–20 μV K^{-1} lower than those of the flat region. This is predictable since metallic Al possesses much lower Seebeck coefficient than YbAl$_3$ does.[27] In addition, some individual points showed large deviations from the average value, which are artifacts originated from the bad contact between the probe and the thin film as caused by the film defects such as pores.

The room-temperature transport properties of YbAl$_3$ thin films are listed in Table 1. The carrier concentration n increases with increasing the annealing temperature. The raise in n should be related to the variation of stoichiometric composition. The Al/Yb atomic ratio of thin films decreases from 3.75 to
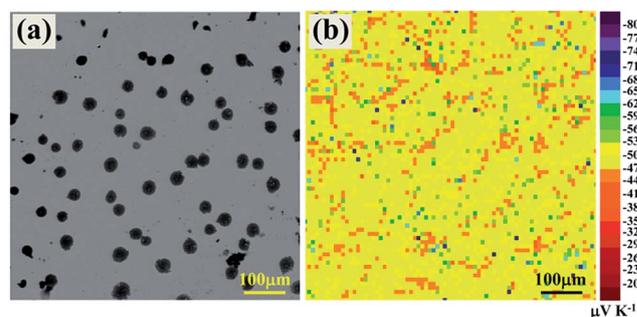

Fig. 5 Cross-sectional FESEM images of YbAl$_3$ thin films before and after annealing treatment. (a) BF673, (b) AF723, (c) AF773, and (d) AF823.

Fig. 6 (a) Backscattered electron image of the surface of AF773 thin film and (b) the distribution of Seebeck coefficient in the same area.

2.90, which means the increased Al vacancies due to Al precipitation on the film surface.[28] Hall mobility μ_H decreases with the annealing temperature, varied in an opposite trend to n. The decreased μ_H should originate from the enhanced carrier scattering from electron–electron interactions, structural defects such as pores, and large surface roughness.[29] The μ_H values of YbAl$_3$ thin films are lower than that of the bulk materials,[19] which is probably due to the existence of nanostructures and rough surfaces.

The temperature dependences of σ, α, and $\alpha^2\sigma$ for the YbAl$_3$ thin films before and after annealing treatment are shown in Fig. 7. The thin films have very high σ values, which are caused by the high n because of the extremely high density of states near the Fermi level derived from the Yb 4f electrons. σ decreases with increasing the measuring temperature in the range of 300–440 K, indicative of the metallic transport behavior. The reduction in σ originates from the enhanced carrier scattering from lattice at elevated temperatures. The room-temperature σ increases from 1.06×10^6 S m^{-1} for the BF673 thin film to 1.69×10^6 S m^{-1} for the AF773 thin film, and then decreases slightly as the annealing temperature is further increased. The increase in σ after annealing treatment is closely relevant to the increased n while the decrease in σ at higher annealing temperatures is a response to the reduced μ_H.

The absolute α is only 30.8 μV K^{-1} before annealing and substantially improved with increasing the annealing temperature in the range of 723–773 K, which is closely related to the significantly improved crystallinity and stoichiometry. At higher annealing temperatures, the absolute α starts to decrease, which should be relevant to the increased n, increased concentration of defects, and reduced crystallinity.[30] The highest absolute α reaches 66.0 μV K^{-1} for the AF773 thin film, which is slightly lower than the value of the highly crystalline YbAl$_3$ bulk materials (about 80.0 μV K^{-1}).[18] Higher absolute α is achievable if the crystallinity of thin films could be improved further. Accordingly, the $\alpha^2\sigma$ value is significantly improved at first with increasing the annealing temperature in the range 723–773 K and then decreases above 773 K. The maximum $\alpha^2\sigma$ is 7.4 mW m^{-1} K^{-2} for the AF773 thin film, which is much higher than the reported values of other promising TE thin films.[30–34] Benefiting from the high electrical conductivity and large power factor, it's expected that the miniaturized TE devices made by YbAl$_3$ thin films have potentially large cooling capacity, large output power, and small Joule heat.

Note that the temperature dependence of electrical conductivity for AF723, AF748, and AF773 thin films shows a bump around 360 K. The decrease of electrical conductivity with temperature becomes more rapid above 360 K. Accordingly, the temperature dependence of Seebeck coefficient also shows abnormal change around 360 K. All these features might be an indication that the Kondo temperature of the annealed YbAl$_3$ thin films is around 360 ± 30 K. The Kondo temperature of 400 K has been reported on a bulk YbAl$_3$ sample.[35]

Unlike the most of semiconducting TE materials in which the contribution of κ is mainly from the lattice component, in YbAl$_3$ the electronic component contributes largely to the total κ owing to its extraordinarily high σ.[18] Therefore, it is possible to estimate κ of YbAl$_3$ thin films using the calculated κ_E and an averagely high κ_L obtained on the bulk materials. Fig. 7d and e shows the calculated κ_E and estimated κ for YbAl$_3$ thin films. Here, κ_E was calculated from σ according to Wiedemann–Franz law. The reported κ_L values (*e.g.* 4.9 W m^{-1} K^{-1} at 300 K) of a typical bulk
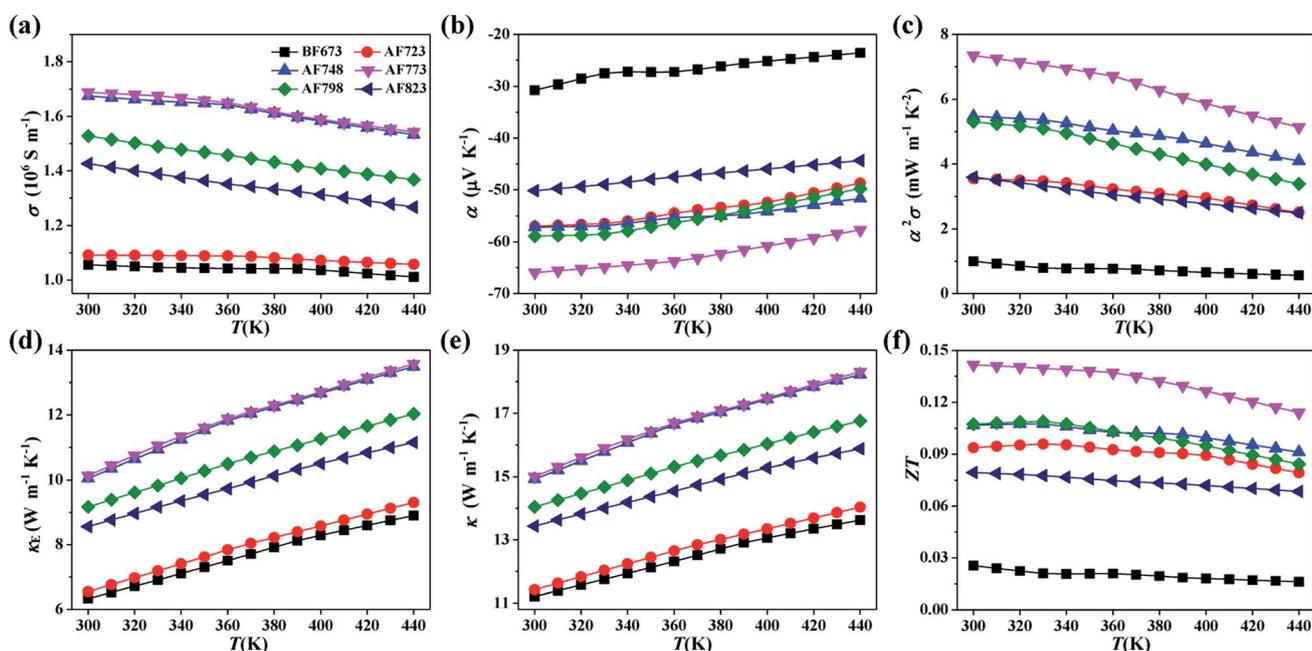

Fig. 7 Temperature dependences of (a) electrical conductivity, (b) Seebeck coefficient, (c) power factor, (d) electronic thermal conductivity, (e) estimated thermal conductivity, and (f) estimated *ZT* for YbAl$_3$ thin films.

material were incorporated to estimate κ.[22] The κ values are over $10\ \mathrm{W\ m^{-1}\ K^{-1}}$ with a large contribution from electrons. Therefore, consideration should be taken in designing TE devices since a large κ is not favorable for building large temperature difference.[12] The ZT values can be estimated from $\alpha^2\sigma$ and κ, and the results are given in Fig. 7f. The thin film annealed at 773 K exhibits the highest ZT of 0.14 at 300 K, which is much higher than that of the thin film without annealing treatment (only 0.03) and is comparable with the values of $YbAl_3$ bulk materials (from 0.17 to 0.24).[18,19] The significant enhancement in TE properties should be attributed to the largely improved $\alpha^2\sigma$ due to the significantly improved crystallinity and stoichiometry. In fact, the ZT values of $YbAl_3$ thin films must be underestimated since the κ_L values of $YbAl_3$ thin film should be lower than those of the bulk materials due to additional phonon scattering from nanostructures, amorphous phases, and rough surfaces.

Conclusions

Intermetallic $YbAl_3$ thermoelectric thin films have been prepared using a co-sputtering technique and a subsequent annealing treatment. The as-prepared thin films had low crystallinity and contained nanoparticles with 30 nm in diameter. After annealing treatment, the crystallization and aggregation of $YbAl_3$ nanoparticles led to significantly improved crystallinity. The precipitation of metallic Al on the surface was favorable for attaining stoichiometric $YbAl_3$ thin films. The electrical conductivity and Seebeck coefficient were improved simultaneously at optimized annealing temperature 773 K, which gave rise to a maximum power factor of $7.4\ \mathrm{mW\ m^{-1}\ K^{-2}}$. The largest ZT of the annealed $YbAl_3$ thin film was estimated to be comparable with those of the bulk materials.

Acknowledgements

References

1 G. Slack, in *CRC Handbook of Thermoelectrics*, ed. D. M. Rowe, CRC Press, Boca Raton, FL, 1995.

2 X. L. Su, P. Wei, H. Li, W. Liu, Y. G. Yan, P. Li, C. Q. Su, C. J. Xie, W. Y. Zhao, P. C. Zhai, Q. J. Zhang, X. F. Tang and C. Uher, *Adv. Mater.*, 2017, DOI: 10.1002/adma.201602013.

3 G. J. Snyder and E. S. Toberer, *Nat. Mater.*, 2008, 7, 105–114.

4 X. F. Tang, W. J. Xie, H. Li, W. Y. Zhao, Q. J. Zhang and M. Niino, *Appl. Phys. Lett.*, 2007, 90, 012102.

5 M. Saleemi, M. S. Toprak, S. H. Li, M. Johnsson and M. Muhammed, *J. Mater. Chem.*, 2012, 22, 725–730.

6 X. Shi, J. Yang, J. R. Salvador, M. F. Chi, J. Y. Cho, H. Wang, S. Q. Bai, J. H. Yang, W. Q. Zhang and L. D. Chen, *J. Am. Chem. Soc.*, 2011, 133, 7837–7846.

7 C. G. Fu, S. Q. Bai, Y. T. Liu, Y. S. Tang, L. D. Chen, X. B. Zhao and T. J. Zhu, *Nat. Commun.*, 2015, 6, 8144.

8 J. P. Heremans, V. Jovovic, E. S. Toberer, A. Saramat, K. Kurosaki, A. Charoenphakdee, S. Yamanaka and G. J. Snyder, *Science*, 2008, 321, 554–557.

9 L. D. Zhao, H. J. Wu, S. Q. Hao, C. I. Wu, X. Y. Zhou, K. Biswas, J. Q. He, T. P. Hogan, C. Uher, C. Wolverton, V. P. Dravid and M. G. Kanatzidis, *Energy Environ. Sci.*, 2013, 6, 3346–3355.

10 J. B. Zhao, Z. X. Liu, J. Reid, K. Takarabe, T. Iida, B. Wang, U. Yoshiya and J. S. Tse, *J. Mater. Chem. A*, 2015, 3, 19774–19782.

11 Z. L. Du, T. J. Zhu, Y. Chen, J. He, H. L. Gao, G. Y. Jiang, T. M. Tritt and X. B. Zhao, *J. Mater. Chem.*, 2012, 22, 6838–6844.

12 T. Huesgen, P. Woias and N. Kockmann, *Sens. Actuators, A*, 2008, 145–146, 423–429.

13 J. H. Bahk, H. Y. Fang, K. Yazawa and A. Shakouri, *J. Mater. Chem. C*, 2015, 3, 10362–10374.

14 R. Venkatasubramanian, E. Siivola, T. Colpitts and B. O'Quinn, *Nature*, 2001, 413, 597–602.

15 K. J. Shin and T. S. Oh, *J. Electron. Mater.*, 2015, 44, 2026–2033.

16 W. Seifert and V. Pluschke, *Phys. Status Solidi B*, 2014, 251, 1416–1425.

17 Q. H. Zhang, X. Y. Huang, S. Q. Bai, X. Shi, C. Uher and L. D. Chen, *Adv. Energy Mater.*, 2015, 18, 194–213.

18 D. Q. He, W. Y. Zhao, X. Mu, H. Y. Zhou and Q. J. Zhang, *J. Electron. Mater.*, 2015, 44, 1919–1925.

19 J. Q. Li, X. Y. Liu, Y. Li, S. H. Song, F. S. Liu and W. Q. Ao, *J. Alloys Compd.*, 2014, 600, 8–12.

20 T. He, T. G. Calvarese, J. Z. Chen, H. D. Rosenfeld, R. J. Small, J. J. Krajewski and M. A. Subramanian, *24th International Conference on Thermoelectrics*, 2005, pp. 434–439.

21 A. D. Christianson, V. R. Fanelli, J. M. Lawrence, E. A. Goremychkin, R. Osborn, E. D. Bauer, J. L. Sarrao, J. D. Thompson, C. D. Frost and J. L. Zarestky, *Phys. Rev. Lett.*, 2006, 96, 117206.

22 G. J. Lehr and D. T. Morelli, *J. Electron. Mater.*, 2013, 42, 1697–1701.

23 H. Miyazaki, *Vacuum*, 2008, 83, 416–418.

24 B. B. He, *Two-dimensional X-ray diffraction*, John Wiley & Sons, Hoboken, 2009.

25 N. W. Ritchie, *Microsc. Microanal.*, 2009, 15, 454–468.

26 S. L. Lai, J. R. A. Carlsson and L. H. Allen, *Appl. Phys. Lett.*, 1998, 72, 1098–1100.

27 S. Kasap, *Thermoelectric Effects in Metals: Thermocouples*, An e-Booklet, 2001.

28 J. Zhou, B. S. Sa and Z. M. Sun, *Intermetallics*, 2010, 18, 2394–2398.

29 D. Huang, F. Yun, M. A. Reshchikov, D. Wang, H. Morkoc, D. L. Rode, L. A. Farina, C. Kurdak, K. T. Tsen, S. S. Park and K. Y. Lee, *Solid-State Electron.*, 2001, 45, 711–715.

30 T. C. Harman, M. P. Walsh, B. E. Laforge and G. W. Turner, *J. Electron. Mater.*, 2005, **34**, 19–22.

31 S. R. Sarath Kumar, A. Alyamani, J. W. Graff, T. M. Tritt and H. N. Alshareef, *J. Mater. Res.*, 2011, **26**, 1836–1841.

32 C. Schumacher, K. G. Reinsberg, R. Rostek, L. Akinsinde, S. Baessler, S. Zastrow, G. Rampelberg, P. Woias, C. Detavernier, J. A. C. Broekaert, J. Bachmann and K. Nielsch, *Adv. Energy Mater.*, 2013, **3**, 95–104.

33 H. C. Chang, T. H. Chen, W. T. Whang and C. H. Chen, *J. Mater. Chem. A*, 2015, **3**, 10459–10465.

34 X. Mu, H. Y. Zhou, D. Q. He, W. Y. Zhao, P. Wei, W. T. Zhu, X. L. Nie, H. J. Liu and Q. J. Zhang, *Nano Energy*, 2017, **33**, 55–64.

35 L. H. Tjeng, S.-J. Oh, E.-J. Cho, H.-J. Lin, C. T. Chen, G.-H. Gweon, J.-H. Park, J. W. Allen, T. Suzuki, M. S. Makivic and D. L. Cox, *Phys. Rev. Lett.*, 1993, **71**, 1419–1422.